Ming Chiu, Tak W. Kee and David M. Huang

Coarse-grained simulations of the effects of chain length, solvent quality, and chemical defects on the solution-phase morphology of MEH-PPV conjugated polymers

Australian Journal of Chemistry, 2012; 65(5):463-471

Originally Published at: http://dx.doi.org/10.1071/CH12029

Coarse-grained simulations of the effects of chain length, solvent quality, and chemical defects on the solution-phase morphology of MEH-PPV conjugated polymers

Ming Chiu[A], *Tak W. Kee*[A], *and David M. Huang*[A,B]

[A] School of Chemistry & Physics, The University of Adelaide, SA 5005, Australia

[B] Email: david.huang@adelaide.edu.au

A mesoscale coarse-grained model of the conjugated polymer poly(2-methoxy-5-(2′-ethylhexyloxy)-1,4-phenylenevinylene) (MEH-PPV) in implicit solvent is developed. The model is parametrized to reproduce the local structure and dynamics of an atomistic simulation model and accounts for solvent quality and saturation chemical defects on the polymer structure. Polymers with defect concentrations of 0 to 10% are simulated using Langevin dynamics in tetrahydrofuran (THF) and in a model poor solvent for chain lengths and solution concentrations used experimentally. The polymer chains are extended in THF and collapse into compact structures in the poor solvent. The radius of gyration decreases with defect content in THF and agrees quantitatively with experiment. The structures formed in poor solvent by chains with 300 monomer units change from toroidal to cylindrical with increasing defect content, while chains containing 1000 monomers form cylinders regardless of defect content. These results have implications for energy transfer in MEH-PPV.

Introduction

Conjugated polymers have attracted widespread and growing interest because of their semiconducting and fluorescent properties and compatibility with low-cost solution-phase processing methods. Among other applications, they have been used in light-emitting diodes,[1] field-effect transistors,[2] solar cells,[3] and fluorescent probes.[4] Poly(2-methoxy-5-(2′-ethylhexyloxy)-1,4-phenylenevinylene) (MEH-PPV), a derivative of poly(*p*-phenylenevinylene) (PPV), is one of the most widely used and extensively studied conjugated polymers.[5,6] MEH-PPV has received particular attention because of its high fluorescence quantum yield and solubility in common organic solvents.

The optical and electronic properties of conjugated polymers are sensitive to the polymer morphology in the solution-cast thin films used in most applications; the morphology in turn depends on the polymer conformations in the solution phase.[7,8] The performance of devices based on conjugated polymers such as solar cells therefore depends sensitively on the morphology.[9] Understanding the solution-phase morphology is particularly important for biological imaging applications,[4,10] in which compact conjugated polymer nanoparticles, prepared by adding a polymer solution to a poor solvent, act as fluorescent probes.

Conjugated polymers such as MEH-PPV can be described as an ensemble of quasi-localized chromophores or conjugated segments, whose length and spatial arrangement govern absorption, fluorescence, and energy transport in these materials.[8,11,12] Electron localization in chromophore units can result from conformational distortions[13,14] or chemical defects[6,14] in the conjugated polymer backbone, which along with polymer–solvent interactions,[8,15,16] also control the mesoscale morphology of these polymers. Chemical defects are common in PPV-based polymers such as MEH-PPV, in which several percent of monomers contain single-bond ("saturation" or "tetrahedral") defects in which the sp^2-hybridized vinylene carbons in the monomer are replaced by sp^3-hybridized alkyl carbons.[6,17,18] Saturation defects can have a profound impact on the structural and optoelectronic properties of MEH-PPV.[6,8,19]

The morphology and photophysics of MEH-PPV, and their dependence on factors such as chemical defects and solvent quality, have been studied experimentally.[8,13,19–22] But experiments can only probe the molecular-level structure of disordered polymers indirectly. Computer models can help to elucidate conjugated polymer morphology and its impact on electronic processes. Most previous computational studies of MEH-PPV morphology have modelled the polymers either as simple "bead and spring" chains[8,23,24] or as fully atomistic polymers.[12,20,22,25] While the simple models have provided qualitative insight into the roles of chemical defects, chain stiffness, and effective polymer–polymer interactions on the mesoscale morphology, they contain adjustable parameters and thus have limited predictive power. On the other hand, atomistic simulations are only feasible for chain lengths and time scales much shorter than those needed to study the evolution of mesoscale structure.

Systematically coarse-grained simulation models take advantage of the low computational cost of simplified models while capturing many of the molecular-level details of fully atomistic models. In essence, systematic coarse-graining involves mapping collections of atoms from an accurate atomistic model on to a smaller set of sites in the coarse-grained (CG) model and then adjusting the CG interactions to reproduce the local structure[26] or forces[27] in the atomistic model. In this way, systematically coarse-grained models make possible molecular simulations of experimentally relevant system sizes while providing an accurate representation of real experimental systems.

MEH-PPV has been systematically coarse grained previously by Hua and co-workers.[28,29] In their earlier model,[28] each MEH-PPV monomer is represented by a single CG site and so does not resolve conformational distortions that break the polymer backbone conjugation. Their later model[29] represents each monomers as three sites (one for the backbone and one for each of the substituents) and can therefore resolve polymer backbone torsions and π-stacking interac-

tions. However, close inspection of their model parameters reveals equilibrium bond angles that add up to much more than 360° for sites that should lie approximately in the plane around a central backbone site. Furthermore, using molecular dynamics (MD) simulations with their model parameters, we could not reproduce the bond angle probability distributions in their published paper. Furthermore, although they report simulating MEH-PPV polymers containing saturation defects,[29] these defects do not appear to be systematically parametrized in the CG model, or at least no parameters are provided. Saturation defects were also only included every 10 monomer units rather than randomly distributed along the polymer chains, as would be the case in a real polymer, and the effect of the defect content on polymer morphology was not explored.

In this work, we systematically parametrize a CG simulation model of MEH-PPV in implicit tetrahydrofuran (THF) solvent to reproduce the local structure and dynamics measured in small-scale simulations of an atomistic model. We then use the parametrized CG model to study the mesoscale structure and dynamics of polymers with chain lengths similar to those used experimentally, which are too large to simulate atomistically. We address some shortcomings of previously published CG models of MEH-PPV, by reparametrizing unphysical bond-angle potentials and by systematically coarse-graining interactions involving saturation defects. We also simulate polymer chains containing randomly distributed defects and investigate the impact on the polymer morphology of varying the defect content from 0 to 10%. We parametrize our CG model of MEH-PPV in THF, a solvent that has not previously been investigated in CG simulation studies, because this solvent has proved useful for preparing MEH-PPV nanoparticles for use as fluoresecent probes.[4,10] This is because MEH-PPV is moderately soluble in THF but not in water, while THF and water are mutually soluble, and so dispersions of MEH-PPV nanoparticles are readily formed by adding a solution of MEH-PPV in THF to water. We also examine effect on the mesoscale polymer morphology of changing the solvent from THF to a model poor solvent.

Computational Methods

Atomistic Simulations

Atomistic simulation models of MEH-PPV, PPV, and THF were constructed using parameters from the OPLS-AA (optimized potentials for liquid simulations all-atom) force field.[30–32] The OPLS-AA force field has been shown to accurately describe the condensed-phase structural and thermodynamic properties of a variety of organic molecules, including certain conjugated oligomers.[33] It should therefore provide an accurate basis for the CG parametrization in this work.

The chemical structures of MEH-PPV (both with and without a saturation defect), PPV, and THF are depicted in Figure 1. For simplicity only regioregular MEH-PPV, in which the alkoxy substituents occupy equivalent positions on all phenyl rings along the polymer chain, was studied. Definitions of the atom types in the simulation models are given in Figure S1 in the Accessory Publication. The OPLS-AA force field, which includes bonded terms (harmonic bond stretching, harmonic angle bending, and sinusodial torsional energies) and non-bonded terms (short-range van der Waals and long-range Coulombic interactions), and the simulation parameters for the molecules studied in this work, are described in Tables S1–S4 in the Accessory Publication.

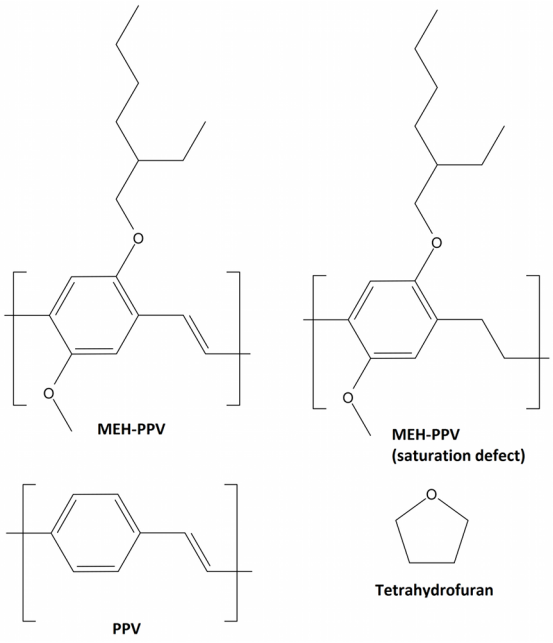

Figure 1: Chemical structures of MEH-PPV, PPV and THF. Polymer chains were terminated by hydrogen atoms on the terminal carbons, whose partial charges were adjusted to enforce electroneutrality.

All systems, including the coarse-grained ones described below, were simulated with the LAMMPS molecular dynamics (MD) simulation package.[34] Unless otherwise stated, atomistic simulations were carried out at constant temperature and pressure (298.13 K and 1 am) using a Nosé-Hoover thermostat[35] and a Nosé-Hoover barostat[36] with a 2-fs time step in a cubic simulation box with periodic boundary conditions. Electrostatic interactions were calculated using the particle–particle particle–mesh (PPPM) method.[37]

Of the bonded interactions, torsions of the polymer backbone are expected to have the greatest impact on the polymer morphology. The OPLS-AA torsional potential for the single bond rotation between the phenylene and vinylene groups of the backbone was therefore reparametrized to account more accurately for this interaction. Specifically, it was parametrized to reproduce the bond rotation energy profile of the central bond in a PPV decamer calculated using density functional theory (DFT) at the B3LYP/6-31G* level.[38] The phenylene–vinylene bond rotation breaks the polymer backbone conjugation and so is energetically costly: the DFT rotation barrier in PPV is over 5 kcal/mol ($> 8k_{\mathrm{B}}T$ at 298 K), substantially higher than that estimated using the OPLS-AA force field, which was not parametrized for molecules with extended conjugated systems. Although higher level quantum chemical calculations of the torsional potential would provide greater quantitative accuracy, such calculations are computationally prohibitive for the chain lengths of roughly 10 monomers needed to achieve convergence in the torsional barriers in conjugated polymers.[39] Furthermore, B3LYP and more accurate coupled-cluster calculations of the inter-monomer torsional potential of bipyrrole agree reasonably well,[40] suggesting that B3LYP is adequate for parametrizing the backbone torsions in classical simulation models of conjugated polymers.

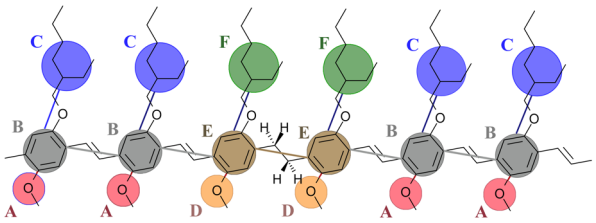

Figure 2: Coarse-graining scheme for an MEH-PPV polymer segment containing a single saturation defect. The CG sites are labelled and CG bonds are shown.

The DFT bond rotation potential $\tilde{U}_{\rm dihed}(\phi)$ implicitly includes interactions between non-bonded atoms. To obtain the "intrinsic" torsional potential $U_{\rm dihed}(\phi)$ that is applied to bonded atom quartets in the simulation force field, the bond rotation potential was estimated in 200-ns constant-temperature gas-phase simulations as $-k_{\rm B}T\ln P_{\rm dihed}(\phi)$, where $P_{\rm dihed}(\phi)$, $k_{\rm B}$, and T are the dihedral angle distribution, Boltzmann constant, and temperature respectively, as detailed elsewhere.[41] The intrinsic torsional potentials of the two carbon backbone dihedral angle involved in this rotation were adjusted until the simulation and DFT bond rotational potentials matched. Although $-k_{\rm B}T\ln P_{\rm dihed}(\phi)$ is strictly a free energy, we have verified in the results presented below that it is insensitive to temperature for simulations at T = 298.13, 373, and 500 K and therefore provides a good approximation for the potential energy. The same intrinsic potential was used for simulating MEH-PPV.

Having parametrized the atomistic models, simulations of MEH-PPV monomers and decamers in THF were carried out to provide the input for the CG model parametrization. Details of the simulated systems are given in Table 1. Statistical averages were only accumulated after the the probability distributions used for the coarse-graining procedure ceased to display systematic variations with time, indicating that the systems had reached equilibrium.

Coarse-Grained Model Parametrization

Following Hua and co-workers,[29] each CG MEH-PPV monomer was modelled using three sites: (A) the center-of-mass (COM) of the methoxy substituent, (B) the COM of the phenylene group, and (C) the COM of the long ethylhexyloxy substituent. In addition, three sites were defined to describe a monomer adjacent to a saturation defect: D, E, and F, which correspond to the same groups of atoms as the A, B and C sites, respectively, on non-defect monomers. Figure 2 illustrates the coarse-graining scheme.

The force field for the interactions between CG sites was parametrized by the iterative Boltzmann inversion (IBI) method[26,41] to reproduce the local structure (radial distribution functions (RDFs) of non-bonded sites and bond, angle, and dihedral distributions) of an equivalent atomistic system. The CG interaction potentials were fit to analytical functions, namely quadratics and 4th-order polynomials for bond lengths, quadratics for bond angles, cosine series for dihedral angles, and Lennard-Jones (LJ) 9-6 potentials for non-bonded interactions. The potential functions and optimized parameters are given in Tables S5–S7 of the Accessory Publication. Non-bonded interactions between defect and non-defect sites were assumed to be the same.

Solvent molecules are computationally expensive to simulate, particularly in the dilute polymer systems that are often studied experimentally. So we did not include solvent molecules explicitly in the CG simulations, but accounted for the effects of the frictional drag and random collisions of solvent molecules on the polymer chains by simulating the polymers dynamics with the Langevin equation,[42]

$$m_i\ddot{\boldsymbol{r}}_i(t) = \boldsymbol{f}_i(t) - m_i\gamma\dot{\boldsymbol{r}}_i(t) + \boldsymbol{\xi}_i(t) \qquad (1)$$

where m_i and $\boldsymbol{r}_i$are the mass and position respectively of particle i, $\boldsymbol{f}_i = -\nabla_i U$ is the conservative force acting on particle i due to the total CG potential energy U, γ is the friction coefficient, and t is time. The random force $\boldsymbol{\xi}_i$ acting on particle i satisfies $\langle\boldsymbol{\xi}_i(t)\rangle = 0$ and $\langle\boldsymbol{\xi}_i(t)\boldsymbol{\xi}_j(t')\rangle = 2\gamma k_{\rm B}Tm_i\delta_{ij}\delta(t-t')$. These equations imply that the random force has no preferred direction and is uncorrelated for different particles and different times. They also ensure that the particle velocities have a Maxwell-Boltzmann distribution at the specified temperature at equilibrium.

Coarse-graining the polymers in implicit solvent to reproduce the structure of atomistic polymers in explicit solvent leads to effective solvent-mediated non-bonded interactions in the CG model. The bonded and non-bonded interactions were optimized respectively in simulations of monomers (systems 1 and 2 in Table 1) and of decamers (systems 3 and 4) in THF at 0.252 g/mL concentration. The accuracy of the CG model was also verified against atomistic simulations of ten-fold less concentrated systems (systems 5 vs 6 and 7 vs 8). The non-defect and defect bonded distributions were optimized for systems of defect-free decamers and systems of decamers containing a single central defect, respectively. The density of the constant-volume CG systems was set to the average density of the corresponding constant-pressure atomistic system. The time step in the CG simulations was 10 fs and the temperature was 298.13 K.

The IBI coarse-graining procedure matches the local structure in the atomistic and CG systems. To match the dynamics in the small-scale simulations, the friction coefficent γ in the Langevin dynamics was set so that the mean squared displacement (MSD) versus time, $\langle r^2(t)\rangle$, was the same in the atomistic and CG monomer simulations at 0.022 g/mL concentration (systems 5 and 6 in Table 1).

Mesoscale Coarse-Grained Simulations

Having parametrized the CG model of MEH-PPV using small-scale systems for which atomistic simulations are feasible, the model was used to simulate experimentally relevant chain lengths (∼1000 monomers) and solution concentrations ($\sim 10^{-4}$ g/mL)[20,21] on times scales (>μs) that allow large-scale aggregation processes to be observed.

A series of simulations of 8 CG polymers with $N_{\rm mon}$ = 300 (system 9) or a single CG polymer with $N_{\rm mon}$ = 1000 (system 10), where $N_{\rm mon}$ is the number of monomers per chain, were carried out using Langevin dynamics at 294.13 K and a concentration of 5.4×10^{-5} g/mL. The initial configuration of the polymer chain was created such that the inter-monomer dihedral distributions matched those measured for defect-free monomers in the optimized small-scale CG simulations described in the previous section. The systems were first simulated at 500 K for 200 ns before quenching to 294.13 K, after which the system was maintained at this temperature.

Langevin dynamics has been found to underestimate the dynamics of large nanoparticles in implicit solvent,[43] because it neglects hydrodynamics, resulting in a scaling of the diffusion coefficient with the inverse particle molecular

Table 1: Details of simulated systems (N_{mon} = no. of monomers per chain; $N_{\mathrm{MEH-PPV}}$ = no. of chains; N_{THF} = no. of THF molecules; L = simulation box length).

System	N_{mon}	$N_{\mathrm{MEH-PPV}}$	N_{THF}	Atomistic/CG	L (Å)[A]	Concentration (g/mL)	Time (ns)
1	1	300	2700	atomistic	80.3	0.252	30
2	1	300	2700	CG	80.3	0.252	30
3	10	30	2700	atomistic	79.7	0.252	50
4	10	30	n/a	CG	79.7	0.252	50
5	1	20	2700	atomistic	73.1	0.022	30
6	1	20	n/a	CG	73.1	0.022	30
7	10	2	2700	atomistic	73.0	0.022	50
8	10	40	n/a	CG	200.8	0.022	50
9	300	8	n/a	CG	2678	5.4×10^{-5}	1500
10	1000	1	n/a	CG	2000	5.4×10^{-5}	2000-6000

[A] This is an average in constant-pressure simulations.

weight ($D \propto M^{-1}$) rather with the inverse particle radius ($D \propto R^{-1}$) predicted by the Stokes–Einstein relation. To approximate the correct mesoscale dynamics of long polymer chains, we have scaled the friction coefficient γ in these mesoscale simulations by $M^{-1/2}$ from the value used in the small-scale decamer simulations. This gives the correct $D \propto R^{-1}$ scaling for a polymer in a θ-solvent, in which $R \propto M^{1/2}$, since the diffusion coefficient D is approximately proportional to γ^{-1} in Langevin dynamics simulations. Although a quantitative treatment of polymer dynamics in solution should account for hydrodynamic interactions, the focus of this paper is the equilibrium structure of MEH-PPV polymers rather than their dynamics, for which the approximate treatment using Langevin dynamics should be adequate. Hydrodynamic interactions can be incorporated into the simulations without modifying the coarse-grained force field that we have developed for MEH-PPV, for example by augmenting the Langevin equation of motion to include the Rotne-Prager-Yamakawa (RPY) tensor.[44,45]

Optical[6,8] and NMR[18] spectroscopy of MEH-PPV have indicated a typical saturation defect concentration of ∼5%. Thus, chains concentrations of randomly assigned saturation defects around this value (0, 5, and 10%) were simulated in this work. The effect of solvent quality was also simulated by increasing the strength of the effective non-bonded interactions between CG polymer sites for THF by a factor of 1.5. THF is a moderately good solvent for MEH-PPV, leading to extended polymer conformations in this solvent; increasing the strength of the non-bonded interactions mimics a poorer solvent, in which the polymer chain should adopt a more compact structure. Details of the simulations that were undertaken are given in Table 1.

Results and Discussion

Atomistic Polymer Backbone Bond Rotation Energy

Figure 3 shows the total intrinsic torsional potential of the phenylene–vinylene single-bond rotation in PPV, which was parametrized to reproduce the bond rotation potential from DFT calculations.[38] The figure shows the close match between the DFT and simulation bond rotation energy profiles. The intrinsic potential was partitioned equally between the two carbon backbone dihedral angles involved in this rotation. The parameters for the intrinsic potential, which were assumed to be the same for PPV and MEH-PPV, are given in Table S4 of the Accessory Publication. We expect that this new parametrization of the backbone bond rotation energy, which is based on quantum chemical calculations, provides a better description than previous atomistic models of the conformational energetics of PPV and its derivatives.

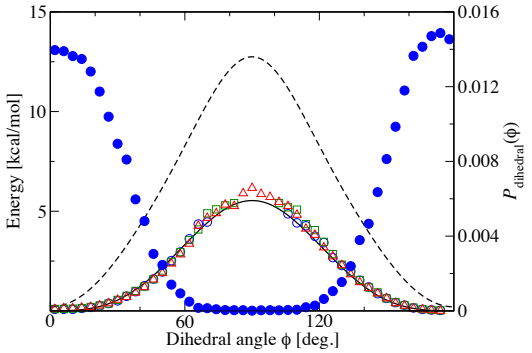

Figure 3: Potential energy profile for rotation of the central phenylene–vinylene single bond in a PPV decamer ($\phi = 0$ corresponds to the configuration in Figure 1) from DFT calculations[38] (solid line) and estimated as $-k_{\mathrm{B}}T \ln P_{\mathrm{dihed}}(\phi)$ from constant-temperature gas-phase simulations (empty symbols) at 298.13 K (circles), 373 K (squares), and 500 K (triangles) in which the total applied "intrinsic" potential was the dashed line. The simulated dihedral probability distribution $P_{\mathrm{dihed}}(\phi)$ at 298.13 K is shown as filled circles.

Coarse-Graining MEH-PPV

The CG model was parametrized to reproduce the local structure and dynamics of the atomistic simulation model. Six CG non-bonded pair interactions, three bonds, six angles, and nine dihedrals in the non-defect segments and an additional bond, five angles, and nine dihedrals in the defect-containing segments of MEH-PPV were parametrized, according to the coarse-graining scheme in Figure 2. As an illustration of the matching of the atomistic and CG structural distributions, the atomistic and CG radial distribu-

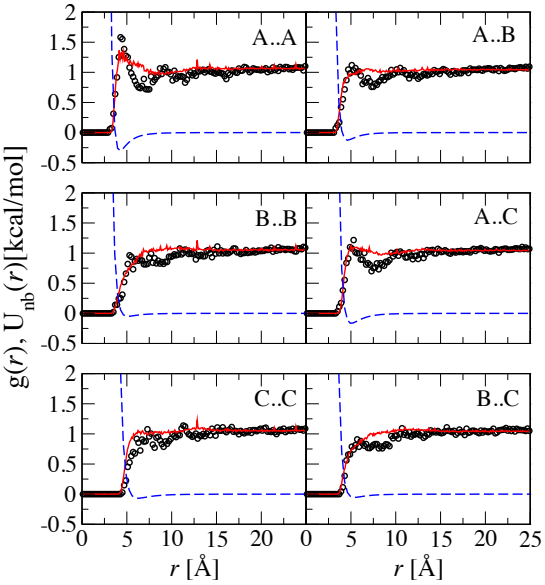

Figure 4: Radial distribution function $g(r)$ for non-bonded sites computed from an atomistic simulation (solid lines) of 0.252 g/mL MEH-PPV monomers in THF at 298.13 K and 1 atm and from a CG simulation (dotted lines) of an equivalent system with optimized CG interaction potentials $U_{\rm nb}(r)$ (dashed lines). Site definitions are shown in Figure 2.

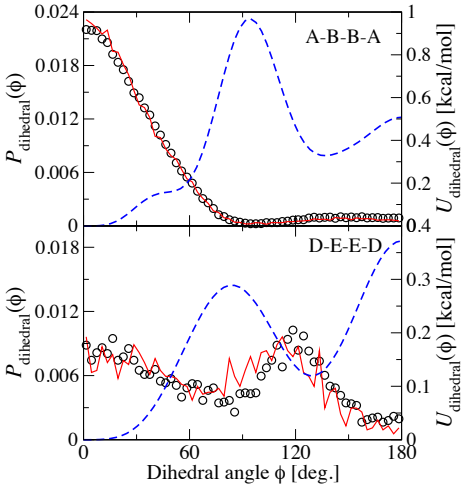

Figure 5: Dihedral angle distributions $P_{\rm dihed}(\phi)$ for the non-defect A-B-B-A and defect D-E-E-D dihedrals computed from atomistic simulations (circles) of 0.252 g/mL MEH-PPV decamers in THF at 298 K and 1 atm (circles) and from CG simulations (solid lines) of an equivalent system with optimized CG potentials $U_{\rm dihed}(\phi)$ (dashed lines). Site definitions are shown in Figure 2.

tion functions (RDFs) and optimized CG pair potentials for the non-bonded interactions are shown in Figure 4 and the atomistic and CG dihedral distributions and optimized CG dihedral potentials for one each of the non-defect and defect dihedrals are shown in Figure 5 for a polymer concentration of 0.252 g/mL. The rest of the distributions and optimized CG potentials are given in Figures S3–S8 of the Accessory Publication.

Despite the simple functional forms used for the CG interaction potentials (Table S5 of the Accessory Publication), the agreement between the atomistic and CG descriptions is reasonably good in all cases. The short-range oscillations in the atomistic RDFs shown in Figure 4, which are due to layering of monomer and solvent molecules, are not captured by the CG model because of solvent molecules were not explicitly in the CG model, but the overall shape of the atomistic RDF is reproduced.

The non-defect A-B-B-A dihedral distributions in Figure 5 for both the atomistic and CG models indicate that substituents of the same type lie predominantly on the same side of the polymer backbone in defect-free chain segments (*syn* conformation) rather than on opposite sides (*anti* conformation). This finding agrees with atomistic Monte Carlo and MD simulations of MEH-PPV oligomers using the PCFF force field,[12] and has been attributed to the greater steric repulsion between the alkoxyl substituents and hydrogens on the vinylene group in the *anti* conformer.[12] The PCFF force field has been shown to give good agreement with ab initio torsional energies for *trans*-stilbene,[12] which is chemically related to PPV and MEH-PPV. On the other hand, our result is opposite to that found in the only previous CG modelling study to include separate CG sites for the backbone and substituents in MEH-PPV; this work used the atomistic DREIDING force field[46] as the basis for the CG parametrization.[29]

Comparison of the non-defect A-B-B-A and corresponding defect D-E-E-D dihedral distributions in Figure 5 shows that introducing defects results in a large increase in the conformational flexibility of the polymer chain, as indicated by the relatively flat D-E-E-D dihedral distribution. All of the other bonded distributions involving defect sites are also broadened compared with the corresponding defect-free distributions (see Figures S3–S8 in the Accessory Publication). In the next section, we examine the consequences of the increased conformational flexibility due to saturation defects on the mesoscale morphology of long polymer chains.

We have also verified that the CG model, which was parametrized at a solution concentration of 0.252 g/mL (systems 1–4), reproduces the atomistic distributions equally well for systems 10 times more dilute (systems 5–8). The RDFs for the dilute atomistic and CG monomers are given in Figure S2 of the Accessory Publication; the corresponding bonded distributions are almost identical to those of the concentrated systems and so are not shown.

The dynamics in the small-scale CG simulations was parametrized by adjusting the Langevin friction coefficient γ to $(95\ {\rm fs})^{-1}$ to match the MSD in the atomistic simulations for the 0.022-g/mL monomer system (systems 5 and 6). We also verified that this value of γ reproduces the atomistic MSDs for different chain lengths and concentrations, as shown in Figure 6. The monomers diffuse faster than decamers at a given concentrations, as expected from the inverse relationship between the diffusion coefficient D and particle radius R in the Stokes–Einstein relation, $D = k_{\rm B}T/(6\pi\eta R)$, where η is the viscosity.[47] The rate of diffusion decreases with concentration, as expected from the increase in η with polymer concentration.[47] The CG structural distributions shown in Figure 4 and 5 and in the Accessory Publication were obtained using this value of γ.

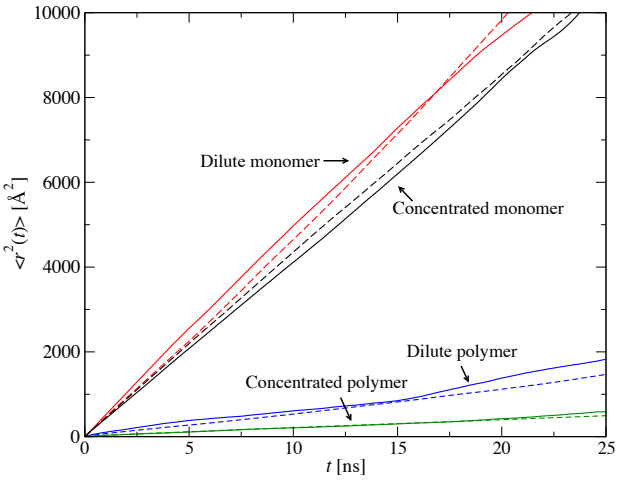

Figure 6: Mean-squared displacement (MSD) of atomistic (solid lines) and CG (dashed lines) monomers and decamers in THF at concentrations of 0.022 g/mL (dilute) and 0.252 g/mL (concentrated). The friction coefficient in the CG simulations was $\gamma = (95\ \text{fs})^{-1}$.

In any case, it was found that the choice of γ (for values up to 10 times larger) did not significantly affect the calculated structural probability distributions.

Impact of Solvent and Defects on Mesoscale Morphology

Figures 7 and 8 depict typical simulation configurations of MEH-PPV polymers with 300 and 1000 monomers, respectively, per chain for different defect concentrations and solvent conditions. For both chain lengths, the polymers have extended configurations in THF. In the simulation trajectories, chain segments were found to come together transiently in THF, but they inevitably came apart again. These results are consistent with experiments,[4,10] which indicate that THF is a reasonable, but not very good, solvent for MEH-PPV at room temperature. The extended chain configurations in THF are qualitatively similar for chains with different defect concentrations, although kinks are evident at the positions of the saturation defects, where the chains have greater conformational flexibility. The difference between the chain configurations was quantified in terms of the radius of gyration R_g, which was calculated using

$$R_\text{g}^2 = \frac{1}{N_\text{mon}} \sum_{i=1}^{N_\text{mon}} |\boldsymbol{r}_i - \boldsymbol{r}_\text{com}|^2 \ , \qquad (2)$$

where $\boldsymbol{r}_i$ and $\boldsymbol{r}_\text{com}$ are the coordinates of monomer i and the polymer centre-of-mass, respectively. The root-mean-squared (RMS) radius of gyration, $\langle R_\text{g}^2 \rangle^{1/2}$, decreases slightly with defect content for the 1000-monomer chains from 45 to 41 nm for 0 to 10% defects. The calculated radius of gyration of the 10%-defect polymers agrees with the measured hydrodynamic radius R_h of 29.5 nm for MEH-PPV chains with $N_\text{mon} \approx 1000$ in THF,[20] using the relationship that $R_\text{g}/R_\text{h} \approx 1.3$ for linear monodisperse polymers in a θ-solvent.[47]

In the poor solvent, the polymer chains aggregrate into compact structures. For the shorter 300-monomer chains, the aggregated structures change qualitatively with defect

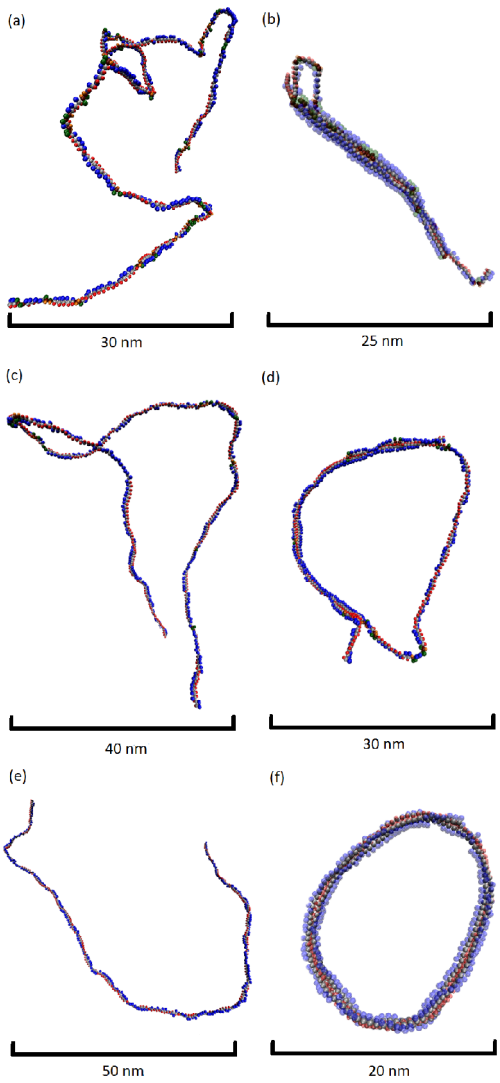

Figure 7: Snapshots of typical simulation configurations of CG polymers with $N_\text{mon} = 300$ for defect concentrations of (a) 10%, (c) 5%, and (e) 0% in THF and (b) 10%, (d) 5% and (f) 0% in the model poor solvent.

concentration. The 0%-defect chains form toroidal structures roughly 20 nm in diameter, while the 10%-defect chains form cylindrical structures roughly 30 nm long. The 5%-defect chains form both toroids and cylinders (only the toroid is shown in Figure 7), with the cylinders roughly twice as long and consisting of half as many loops as in the 10%-defect case. On the other hand, the aggregated structures are qualitatively similar for the longer 1000-monomer chains with 0% and 10% defect concentrations, with cylinders formed in both cases. The loops formed by the longer chains with 0% defects are slightly wider than those with 10% defects, due to the higher stiffness of the non-defect chain segments.

The results for the 300-monomer chains are qualitatively consistent with those of Monte Carlo simulations of 0%- and 6%-defect 250-monomer chains using a simple lattice model of MEH-PPV. In this model, each 2.5 monomers was represented by a single site and model parameters were simply set to physically reasonable values.[8] These simulations found distinct toroidal and cylindrical structures respectively for

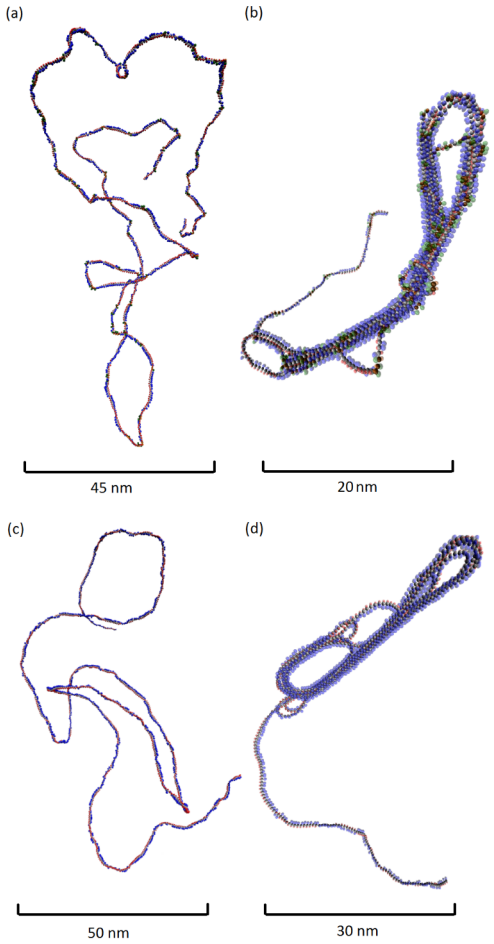

Figure 8: Snapshots of typical simulation configurations of CG polymers with $N_{\mathrm{mon}} = 1000$ for defect concentrations of (a) 10% and (c) 0% in THF and (b) 10% and (d) 0% in the model poor solvent.

0% and 6% defects. The so-called "defect cylinder" structure formed by the 6%-defect chains was found to match the distribution of modulation depths from single-molecule polarization spectroscopy experiments.[8] Our results for chain lengths of 1000, which is more typical of the chain lengths used experimentally, suggest that longer chains with 1000 or more monomers form similar aggregated structures in poor solvent for defect contents up to 10%. Such chains are many times longer than the persistence length, even for defect-free segments, and so they are less constrained in the way they aggregate than the shorter 300-monomer chains. Thus, regardless of defect concentration, they can loop back on themselves to form compact cylindrical structures in which adjacent chain segments are parallel to each other, with some difference in the curvature of the loops at the ends of the cylinders depending on the defect concentration. The persistence length l_{p} was estimated from $l_{\mathrm{p}} = 3R_{\mathrm{g}}^2/R_{\mathrm{max}}$,[13] where R_{max} is the chain contour length, to be 7.7 nm and 9.3 nm or roughly 12 and 14 monomers, respectively, for the 0%- and 10%-defect polymers with $N_{\mathrm{mon}} = 1000$.

These results have implications for energy transfer in MEH-PPV, which is critical for many applications of these polymers, because energy transfer rates are sensitive to the polymer morphology. To a first approximation, energy transfer occurs between quasi-localized chromophore units into which the polymer chain is divided by conformational distortions or chemical defects; the transition dipoles of these chromophores are aligned parallel to the chromophore axis.[48] The transfer rate depends on the absorption and emission spectra of the donor and acceptor chromophores. It also decreases with increasing donor–acceptor distance and as the relative orientation of their transition dipoles changes from parallel to perpendicular. The rate of energy transfer is, not surprisingly, expected to change as a polymer goes from an extended conformation in a good solvent to a compact structure in a poor solvent. Our results also suggest that the energy transfer rates in aggregated structures should be more sensitive to the saturation defect concentration for shorter chains than for longer chains, due to the stronger dependence of the mesoscale polymer morphology on the defect concentration in shorter chains.

The ultimate goal of this work is to elucidate the molecular-level mechanisms for variations in photophysical properties of conjugated polymers such as energy transfer and fluorescence with solvent- or defect-induced changes in the polymer morphology. In work to be published, we couple of CG simulation configurations of MEH-PPV with a morphology-dependent model of energy transfer dynamics between weakly coupled chromophores[49] to achieve this goal.

Conclusions

The systematically coarse-grained model of MEH-PPV that has been developed in this work improves on previously developed models by reparametrizing unphysical bond-angle potentials, by parametrizing inter-monomer torsions using quantum chemical calculations, by systematically coarse-graining saturation defects, and by treating polymers with random rather than regularly spaced defect positions. The model gives good agreement with experiment for the radius of gyration of MEH-PPV in THF. Simulations of MEH-PPV polymers with 300 and 1000 monomers per chain for saturation defect concentrations of 0 to 10% in THF and in a model poor solvent show that the polymers are extended in THF, a moderately good solvent. These extended configurations are qualitatively similar for different defect concentrations, although the radius of gyration decreases slightly with the number of defects. The polymers collapse into compact structures in the poor solvent. The structures formed by the 300-monomer chains change significantly with defect concentration, with toroids formed for 0% defects, cylinders for 10% defects, and a combination of the two for 5% defects, in qualitative agreement with previous simulations of a simple lattice model of MEH-PPV. On the other hand, the 1000-monomer chains form cylinders for both 0 and 10% defect concentrations.

Accessory Publication

The atomistic simulation model parameters for MEH-PPV, PPV, and THF and the coarse-grained simulation model parameters for MEH-PPV in implicit THF are given in the Accessory Publication, which is available from the journal website.

Acknowledgments

Financial support from The University of Adelaide is gratefully acknowledged. This work was supported by an award under the Merit Allocation Scheme on the NCI Na-

tional Facility at the ANU.

References

[1] J. H. Burroughes, D. D. C. Bradley, A. R. Brown, R. N. Marks, K. Mackay, R. H. Friend, P. L. Burns, A. B. Holmes, *Nature* **1990**, *347*, 539.

[2] H. Sirringhaus, N. Tessler, R. H. Friend, *Science* **1998**, *280*, 1741.

[3] J. J. M. Halls, C. A. Walsh, N. C. Greenham, E. A. Marseglia, R. H. Friend, S. C. Moratti, A. B. Holmes, *Nature* **1995**, *376*, 498.

[4] C. Wu, C. Szymanski, J. McNeill, *Langmuir* **2006**, *22*, 2956.

[5] R. H. Friend, R. W. Gymer, A. B. Holmes, J. H. Burroughes, R. N. Marks, C. Taliani, D. D. C. Bradley, D. A. D. Santos, J. L. Bredas, M. Logdlund, W. R. Salaneck, *Nature* **1999**, *397*, 121.

[6] G. Padmanaban, S. Ramakrishnan, *J. Am. Chem. Soc.* **2000**, *122*, 2244.

[7] B. J. Schwartz, *Annu. Rev. Phys. Chem.* **2003**, *54*, 141.

[8] D. Hu, J. Yu, K. Wong, B. Bagchi, P. J. Rossky, P. F. Barbara, *Nature* **2000**, *405*, 1030.

[9] C. J. Brabec, M. Heeney, I. McCulloch, J. Nelson, *Chem. Soc. Rev.* **2011**, *40*, 1185.

[10] S. N. Clafton, D. A. Beattie, A. Mierczynska-Vasilev, R. G. Acres, A. C. Morgan, T. W. Kee, *Langmuir* **2010**, *26*, 17785.

[11] A. Kohler, D. A. dos Santos, D. Beljonne, Z. Shuai, J. L. Bredas, A. B. Holmes, A. Kraus, K. Mullen, R. H. Friend, *Nature* **1998**, *392*, 903.

[12] C. De Leener, E. Hennebicq, J.-C. Sancho-Garcia, D. Beljonne, *J. Phys. Chem. B* **2009**, *113*, 1311.

[13] C. Gettinger, A. J. Heeger, J. Drake, D. Pine, *J. Chem. Phys.* **1994**, *101*, 1673.

[14] K. F. Wong, M. S. Skaf, C.-Y. Yang, P. J. Rossky, B. Bagchi, D. Hu, J. Yu, P. F. Barbara, *J. Phys. Chem. B* **2001**, *105*, 6103.

[15] T.-Q. Nguyen, V. Doan, B. J. Schwartz, *J. Chem. Phys.* **1999**, *110*, 4068.

[16] J. Vogelsang, J. Brazard, T. Adachi, J. C. Bolinger, P. F. Barbara, *Angew. Chem. Int. Ed.* **2011**, *50*, 2257.

[17] H. Becker, H. Spreitzer, K. Ibrom, W. Kreuder, *Macromolecules* **1999**, *32*, 4925.

[18] A. R. Inigo, H.-C. Chiu, W. Fann, Y.-S. Huang, U. S. Jeng, C. H. Hsu, K.-Y. Peng, S.-A. Chen, *Synth. Met.* **2003**, *139*, 581.

[19] P. K. Choudhury, D. Bagchi, C. S. S. Sangeeth, R. Menon, *J. Mater. Chem.* **2011**, *21*, 1607.

[20] P. Kumar, A. Mehta, S. M. Mahurin, S. Dai, M. D. Dadmun, B. G. Sumpter, M. D. Barnes, *Macromolecules* **2004**, *37*, 6132.

[21] S. Habuchi, S. Onda, M. Vacha, *Phys. Chem. Chem. Phys.* **2011**, *13*, 1743.

[22] G. Bounos, S. Ghosh, A. K. Lee, K. N. Plunkett, K. H. DuBay, J. C. Bolinger, R. Zhang, R. A. Friesner, C. Nuckolls, D. R. Reichman, P. F. Barbara, *J. Am. Chem. Soc.* **2011**, *133*, 10155.

[23] Y. Ebihara, M. Vacha, *J. Phys. Chem. B* **2008**, *112*, 12575.

[24] T. Adachi, J. Brazard, P. Chokshi, J. C. Bolinger, V. Ganesan, P. F. Barbara, *J. Phys. Chem. C* **2010**, *114*, 20896.

[25] B. G. Sumpter, P. Kumar, A. Mehta, M. D. Barnes, W. A. Shelton, R. J. Harrison, *J. Phys. Chem. B* **2005**, *109*, 7671.

[26] D. Reith, M. Pütz, F. Müller-Plathe, *J. Comput. Chem.* **2003**, *24*, 1624.

[27] S. Izvekov, G. A. Voth, *J. Chem. Phys.* **2005**, *123*, 134105.

[28] C. K. Lee, C. C. Hua, S. A. Chen, *J. Phys. Chem. B* **2008**, *112*, 11479.

[29] C. K. Lee, C. C. Hua, S. A. Chen, *Macromolecules* **2011**, *44*, 320.

[30] W. L. Jorgensen, D. S. Maxwell, J. Tirado-Rives, *J. Am. Chem. Soc.* **1996**, *118*, 11225.

[31] G. A. Kaminski, R. A. Friesner, J. Tirado-Rives, W. L. Jorgensen, *J. Phys. Chem. B* **2001**, *105*, 6474.

[32] M. L. P. Price, D. Ostrovsky, W. L. Jorgensen, *J. Comput. Chem.* **2001**, *22*, 1340.

[33] V. Marcon, G. Raos, *J. Am. Chem. Soc.* **2006**, *128*, 1408.

[34] S. J. Plimpton, *J. Comput. Phys.* **1995**, *117*, 1, `LAMMPS` Molecular Dynamics Simulator: http://lammps.sandia.gov.

[35] W. G. Hoover, *Phys. Rev. A* **1985**, *31*, 1695.

[36] W. G. Hoover, *Phys. Rev. A* **1986**, *34*, 2499.

[37] R. W. Hockney, J. W. Eastwood, *Computer Simulation Using Particles* **1988** (Taylor & Francis: Bristol).

[38] S. Grimm, D. Tabatabai, A. Scherer, J. Michaelis, I. Frank, *J. Phys. Chem. B* **2007**, *111*, 12053.

[39] S. B. Darling, M. Sternberg, *J. Phys. Chem. B* **2009**, *113*, 6215.

[40] J. C. Sancho-Garca, A. Karpfen, *Chem. Phys. Lett.* **2005**, *411*, 321.

[41] D. M. Huang, R. Faller, K. Do, A. J. Moulé, *J. Chem. Theory Comput.* **2010**, *6*, 526.

[42] M. P. Allen, D. J. Tildesley, *Computer Simulation of Liquids* **1987** (Clarendon: Oxford).

[43] J. R. Spaeth, I. G. Kevrekidis, A. Z. Panagiotopoulos, *J. Chem. Phys.* **2011**, *134*, 164902.

[44] J. Rotne, S. Prager, *J. Chem. Phys.* **1969**, *50*, 4831.

[45] H. Yamakawa, *J. Chem. Phys.* **1970**, *53*, 436.

[46] S. L. Mayo, B. D. Olafson, W. A. Goddard, *J. Phys. Chem.* **1990**, *94*, 8897.

[47] M. Rubinstein, R. H. Colby, *Polymer Physics* **2003** (Oxford University Press: Oxford).

[48] M. M. L. Grage, P. W. Wood, A. Ruseckas, T. Pullerits, W. Mitchell, P. L. Burn, I. D. W. Samuel, V. Sundstrom, *J. Chem. Phys.* **2003**, *118*, 7644.

[49] S. Westenhoff, C. Daniel, R. H. Friend, C. Silva, V. Sundstrom, A. Yartsev, *J. Chem. Phys.* **2005**, *122*, 094903.